



1 **Indirect assimilation of radar reflectivity data with an adaptive**
2 **hydrometer retrieval scheme for the short-term severe weather**
3 **forecasts**

4
5 Lixin Song^{1,2,3}, Feifei Shen^{1,2,4,5*}, Zhixin He⁶, Dongmei Xu¹, Aiqing Shu¹, and Jiajun Chen¹

6
7 ¹ Key Laboratory of Meteorological Disaster, Ministry of Education (KLME) /Joint
8 International Research Laboratory of Climate and Environment Change (ILCEC) /Collaborative
9 Innovation Center on Forecast and Evaluation of Meteorological Disasters (CIC-FEMD), Nanjing
10 University of Information Science & Technology, Nanjing 210044, China

11
12 ² China Meteorological Administration Tornado Key Laboratory

13
14 ³ Department of Atmospheric and Oceanic Sciences and Institute of Atmospheric Sciences,
15 Fudan University, Shanghai 200433, China

16
17 ⁴ China Meteorological Administration Radar Meteorology Key Laboratory, Nanjing 210000,
18 China

19
20 ⁵ Shanghai Typhoon Institute, China Meteorological Administration, Shanghai 200030, China

21
22 ⁶ Anhui Meteorological Observatory, Hefei 230000, China

23
24
25
26 *Corresponding author address:
27 Feifei Shen
28 Nanjing University of Information Science & Technology
29 ffshen@nuist.edu.cn



30

Abstract

31 Different hydrometeor retrieval schemes are explored based on the Weather Research and
32 Forecasting (WRF) model in the indirect assimilation of radar reflectivity for two real cases
33 occurred during June 2020 and August 2018. When retrieving hydrometeors from radar reflectivity,
34 there are two commonly used hydrometeor classification methods: “temperature-based” and
35 “background hydrometer-dependent” schemes. The hydrometeor proportions are usually
36 empirically assigned in the “temperature-based” method within different background temperature
37 intervals. Whereas, in the “background hydrometer-dependent” scheme, each type of the
38 hydrometeor is derived based on the portions estimated from the background field for different radar
39 reflectivity ranges. In this study, a blending scheme is designed to combine “temperature-based”
40 and “background hydrometer-dependent” methods adaptively to avoid errors caused by fixed
41 relationships and reduce uncertainties introduced by the background field itself. Three experiments,
42 EXP_temp, EXP_bg, and EXP_temp-bg are conducted using the “temperature-based” method,
43 “background hydrometer-dependent” scheme, and blending scheme, respectively. It is found that,
44 the blending scheme facilitates the generation of accurate hydrometeor species which will enhance
45 the effectiveness of radar data assimilation. EXP_temp-bg is capable of analyzing radar reflectivity
46 structures more accurately compared to both EXP_temp and EXP_bg. Besides, due to the adaptive
47 combination of “temperature-based” and “background hydrometer-dependent” schemes, the
48 EXP_temp-bg experiment predict the radar reflectivity structures and precipitation intensity more
49 accurately.

50 **Key words:** Numerical weather prediction, Radar data assimilation, Hydrometeor retrieval.

51

52 1. Introduction

53 The initial condition is a crucial factor in enhancing the accuracy of numerical weather prediction
54 (Navon, 2009; Kain et al., 2010; Lopez, 2011; Xu et al., 2021). Compared to conventional
55 observations, doppler radar observations have extremely high temporal and spatial resolution, as
56 well as containing precipitating hydrometeor information (Zhao et al., 2012; Li et al., 2013; Kong
57 et al., 2020). Therefore, radar is one of the key platforms for obtaining proper initial conditions to
58 successfully predict convective storms (Lilly, 1990; Dawson et al., 2015; Gustafsson et al., 2018;



59 Shen et al., 2020a; Xu et al., 2022; Chen et al., 2023). A number of efforts have been devoted to
60 assimilating radar data into mesoscale numerical models (Lindskog et al., 2004; Dowell et al., 2011;
61 Sun et al., 2014; Bick et al., 2016; Tong et al., 2020; Shen et al., 2016, 2019, 2022; Wan et al., 2024).

62 Radar observations have two fundamental variables: radar radial velocity (V_r) and radar
63 reflectivity (Z). Assimilating radar radial velocity is conducive to improving the dynamical structure
64 of the initial field. Numerous scholars are dedicated to researching radar radial velocity assimilation
65 (Gao et al., 2004; Simonin et al., 2014; Li et al., 2016; Shen et al., 2020b). Based on the three-
66 dimensional variational (3DVar) system of the fifth generation Pennsylvania State University-
67 NCAR Mesoscale Model (MM5), Xiao et al. (2005) developed a radar radial velocity observation
68 operator, and investigated the impact of assimilating radar radial velocity on precipitation forecasts.
69 Besides, Wang et al. (2013b) employed the four-dimensional variational (4DVar) system to
70 assimilate radar radial velocity and reflectivity into the model for enhancing forecasting accuracy.

71 In contrast, assimilating radar reflectivity is more challenging than assimilating the radial wind,
72 on account of its highly nonlinear observation operator and close relationship with complex
73 microphysics (Borderies et al., 2019; Xu et al., 2019). Currently, there are two main methods for
74 assimilating radar reflectivity: direct assimilation and indirect assimilation. Xiao et al. (2007)
75 proposed a direct assimilation scheme for radar reflectivity based on the 3DVar system of MM5.
76 The water content was classified according to phases using warm rain microphysical processes.
77 However, due to the absence of ice phase particles, the positive impact is not promising in cases of
78 deep moist convections generated through cold-cloud processes. To assimilate radar reflectivity into
79 numerical weather prediction (NWP) models more effectively, Gao and Stensrud (2012) proposed
80 a hydrometeor classification method based on the 3DVar system in the direct assimilation of radar
81 reflectivity. The results demonstrated that this classification method benefits to accelerate the
82 convergence speed of the analysis and reduce errors in the analysis. Compared to variational data
83 assimilation methods, Ensemble Kalman Filter (EnKF; Evensen, 1994) is a better choice for
84 assimilating radar reflectivity directly, since EnKF does not require consideration of the tangent or
85 adjoint model of the observation operator (Liu et al., 2019). Based on the EnKF method, Tong and
86 Xue (2005) assimilated the simulated radar observations from a supercell storm. The results
87 indicated that directly assimilating radar reflectivity data has a positive impact on both analyses and



88 forecasts. Although the forward operator of reflectivity tends to be easily implemented in EnKF, its
89 computational cost is too high to be widely applied in the scientific research and operational
90 forecasting (Kong et al., 2018).

91 To avoid the issue of high nonlinearity in radar reflectivity observation operators, the indirect
92 assimilation method is often used in the NWP. Based on the Advance Regional Prediction System
93 (ARPS), Hu et al. (2006) investigated the impact of cloud analysis using radar reflectivity on
94 forecasting tornado storms. They found that cloud analysis helps to adjust the temperature, humidity
95 fields, and hydrometeors within the clouds, thereby improving tornado predictions. Also,
96 Schenkman et al. (2011) found that cloud analysis technology is able to adjust cloud variables to
97 better suit the dynamic and thermal fields. However, cloud analysis schemes rely largely on
98 uncertain empirical relationships, thus usually hardly suppressing the generation of spurious echoes.
99 Using the 4DVar system, Sun and Crook (1997) proposed to assimilate rainwater mixing ratios
100 retrieved from reflectivity instead of directly assimilating reflectivity, which seems to produce better
101 analysis results. Based on the 3DVar system of WRF, Wang et al. (2013a) further demonstrated that
102 assimilation of rainwater and estimated water vapor obtained from radar reflectivity reduces the
103 linearization error of the radar reflectivity observation operator, thus improving precipitation
104 forecasts. However, both indirect assimilation methods under the two variational frameworks are
105 employed in the warm-rain scheme, which restricts their applications above troposphere or in the
106 coexistence of liquid and ice particles. Shen et al. (2021) added hydrometeor control variables
107 included ice-phase particles when indirectly assimilating radar reflectivity observations of
108 Hurricane IKE, which enables track and intensity forecasts of the hurricane to be greatly improved.

109 For the indirect assimilation of radar reflectivity, one of the challenges is how to correctly classify
110 hydrometeors in observations. There are currently two methods to distinguish hydrometeor types.
111 One is to classify hydrometeor types according to background temperature (hereafter called
112 temperature-based) developed by Gao and Stensrud (2012), with fixed parameters and empirical
113 relations. Another is the “background hydrometer-dependent” hydrometeor retrieval scheme (Chen
114 et al., 2020, 2021). The “background hydrometer-dependent” method calculates hydrometeor
115 weights in various thresholds from the model background field to better allocate radar reflectivity
116 observation information. This approach avoids empirical thresholds and weighting coefficients



117 given in the “temperature-based” method, and benefits to improve the accuracy of hydrometeor
118 retrievals. However, the “background hydrometer-dependent” scheme also relies on the accuracy of
119 the background field itself. When the background field is similar to the observation, the “background
120 hydrometer-dependent” method tends to provide accurate hydrometeor weights. On the other hand,
121 when the background field differs significantly from the observation, the algorithm may not be
122 suitable for appropriately allocating hydrometeors of the radar reflectivity observation. Considering
123 their own limitations in either “temperature-based” or “background hydrometer-dependent”
124 schemes, this study aims to adaptively combine two above methods of classifying hydrometeors to
125 assimilate radar reflectivity more reasonably.

126 In the study, the WRF-3DVar methods, observation operators, and different retrieval methods are
127 included in the section 2. The section 3 shows experimental designs. The section 4 presents analysis
128 and forecast results of all experiments. The conclusion is presented in the section 5.

129 2. Methods

130 2.1 The WRF-3DVar system

131 Based on the incremental method proposed by Courtier et al. (1994), 3DVar uses the minimization
132 algorithm to solve the objective function. The cost function is as follows:

$$133 \quad J = \frac{1}{2}(\mathbf{x} - \mathbf{x}_b)^T \mathbf{B}^{-1}(\mathbf{x} - \mathbf{x}_b) + \frac{1}{2}[\mathbf{y}_o - \mathbf{H}(\mathbf{x})]^T \mathbf{R}^{-1}[\mathbf{y}_o - \mathbf{H}(\mathbf{x})]. \quad (1)$$

134 The vectors \mathbf{x} , \mathbf{x}_b , and \mathbf{y}_o stand for analysis variables, background variables, and observation
135 variables. \mathbf{B} is the background error covariance, which is calculated by the National
136 Meteorological Center (NMC; Parrish and Derber, 1992) method. \mathbf{R} represents the observation
137 error covariance. \mathbf{H} is the nonlinear observation operator.

138 2.2 The radial velocity observation operator

139 The radial velocity observation operator is as follows:

$$140 \quad V_r = u \frac{x-x_i}{r_i} + v \frac{y-y_i}{r_i} + (w - v_T) \frac{z-z_i}{r_i}. \quad (2)$$

141 u , v , and w denote the zonal, meridional, and vertical wind component, respectively. (x, y, z)
142 and (x_i, y_i, z_i) represent the radar position and observation position, respectively. r_i is the
143 distance between the radar and the observation. v_T is the terminal speed.



144 2.3 The radar reflectivity observation operator

145 According to Tong and Xue (2005), the radar reflectivity observation operator is as follows:

$$146 \quad Z = 10 * \log_{10}(Z_e), \quad (3)$$

$$147 \quad Z_e = Z_e(q_r) + Z_e(q_s) + Z_e(q_g), \quad (4)$$

$$148 \quad Z_e(q_x) = \alpha_x(\rho q_x)^{1.75}. \quad (5)$$

149 q_x means hydrometeor mixing ratios. $Z_e(q_x)$ (units: dBZ) is the equivalent reflectivity factor
150 of rainwater, snow, and graupel. α_x represents the fixed coefficient that is determined by the
151 dielectric coefficient, density and intercept parameter of each hydrometeor. α_r is 3.63×10^9 . For
152 snow and graupel, the coefficient is temperature dependent. When the environmental temperature
153 is greater than 0°C , α_s for wet snow is 4.26×10^{11} and α_g for wet graupel is 9.08×10^9 . When the
154 temperature is below 0°C , α_s for dry snow is 9.80×10^8 and α_g for dry graupel is 1.09×10^9 . ρ is
155 the air density. During the direct assimilation of radar reflectivity, the linearization errors are almost
156 inevitable.

157 The indirect method assimilates the retrieved hydrometeors from the radar reflectivity. Firstly, it
158 is required to determine the proportion of each hydrometeor in radar reflectivity observation. At
159 present, there are two methods to obtain the proportion of each hydrometeor.

160 2.3.1 The “Temperature-based” method

161 In Gao and Stensrud (2012), the hydrometeor types in reflectivity are classified based on the
162 background temperature. The specific values are as follows:

$$163 \quad C_r = 1, C_s = C_g = 0, T_b > 5^\circ\text{C}, \quad (6)$$

$$164 \quad C_r = \frac{T_b+5}{10}, C_s = (1 - C_r) \cdot \frac{\alpha_s}{\alpha_s + \alpha_g}, C_g = (1 - C_r) \cdot \frac{\alpha_g}{\alpha_s + \alpha_g}, -5^\circ\text{C} < T_b < 5^\circ\text{C}, \quad (7)$$

$$165 \quad C_r = 0, C_s = \frac{\alpha_s}{\alpha_s + \alpha_g}, C_g = \frac{\alpha_g}{\alpha_s + \alpha_g}, T_b < -5^\circ\text{C}. \quad (8)$$

166 C_r , C_s , and C_g denote the weights of rainwater, snow, and graupel, respectively. α_r , α_s , and
167 α_g represent the fixed coefficients of rainwater, snow, and graupel, respectively (Same as above).
168 T_b is the background temperature.

169 2.3.2 The “Background hydrometer-dependent” method

170 It is found that hydrometeor weights derived from the background field vary with individual



171 weather conditions, which helps to reduce errors resulting from fixed coefficients in Chen et al.
172 (2020, 2021). The specific process of calculating proportions is as follows:

- 173 (1) Compute the average equivalent radar reflectivity of each hydrometeor in different reflectivity
174 ranges and model layers based on the background field statistics.
- 175 (2) Calculate the weight of each hydrometeor in the background field.
- 176 (3) Divide radar reflectivity observations based on the weights derived from Step 2. If the
177 background field has missing data, the calculated climatological mean for one month will be
178 used instead.

179 2.3.3 The blending method

180 The blending method aims to utilize the two methods of partitioning hydrometeors accordingly
181 to retrieve multi-hydrometer more reasonably in radar reflectivity indirect assimilation. The formulas
182 are as follow:

$$183 \quad \beta = \frac{\delta_t^2}{\delta_t^2 + \delta_b^2}, \quad (9)$$

$$184 \quad C_x = \beta C_x^b + (1 - \beta) C_x^t. \quad (10)$$

185 δ_t^2 represents the deviation between the hydrometeor content of the background field and the
186 retrieved hydrometeor content based on the “temperature-based” scheme. δ_b^2 is the deviation
187 between the hydrometeor content of the background field and the retrieved hydrometeor by the
188 “background hydrometer-dependent” scheme. C_x^t and C_x^b are the weights calculated by the
189 “temperature-based” and “background hydrometer-dependent” methods, respectively.

190 3. Experimental design

191 WRF v4.3 and its data assimilation system WRFDA v4.3 are used in this study. Two convective
192 cases are studied in the study: 14 June in 2020 (called Case 1; Fig. 1a) and 6 August in 2018 (denoted
193 as Case 2; Fig. 1b). The specific applications of physical parametrizations are as follows: the WRF
194 Double-Moment 6-Class Microphysics (WDM6) scheme, the Rapid Radiative Transfer Model
195 (RRTM) long wave radiation scheme (Mlawer et al., 1997), the Dudhia short-wave radiation scheme
196 (Dudhia, 1989), the Yonsei University (YSU) boundary layer scheme (Hong et al., 2006), and the
197 Noah Land Surface Model (Chen and Dudhia, 2001) for land surface process scheme. No cumulus
198 parameterization scheme is employed. As shown in Table 1, three data assimilation (DA)
199 experiments are conducted to evaluate the effects of all retrieval methods in the study. For all three



200 DA experiments, the initial and lateral boundary conditions are provided by the NCEP Global
 201 Forecast System (GFS) data. Besides, the specific flowchart is presented in the Fig. 2.

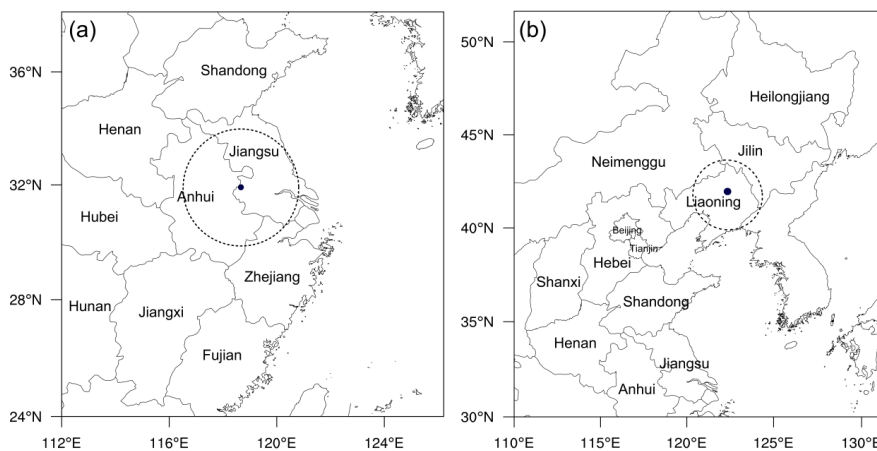
202

203

204

Table 1. The list of DA experiments.

Experiments	Hydrometeor retrieval methods
EXP_temp	The “temperature-based” method
EXP_bg	The “background hydrometer-dependent” method
EXP_temp-bg	The blending method

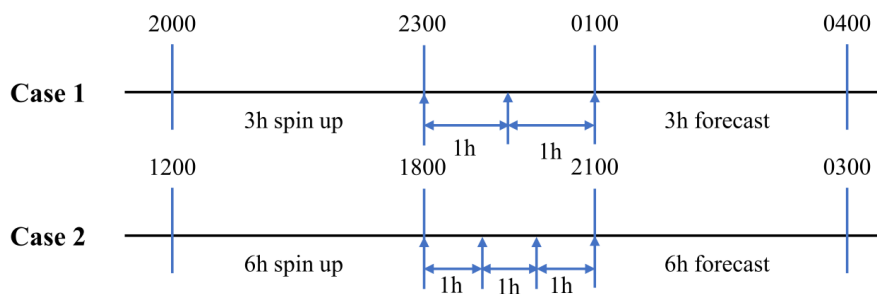


205

206

Fig. 1. The simulated area of (a) Case 1 and (b) Case 2, with the detecting ranges of the Nanjing radar and Shenyang Radar.

207



208

209

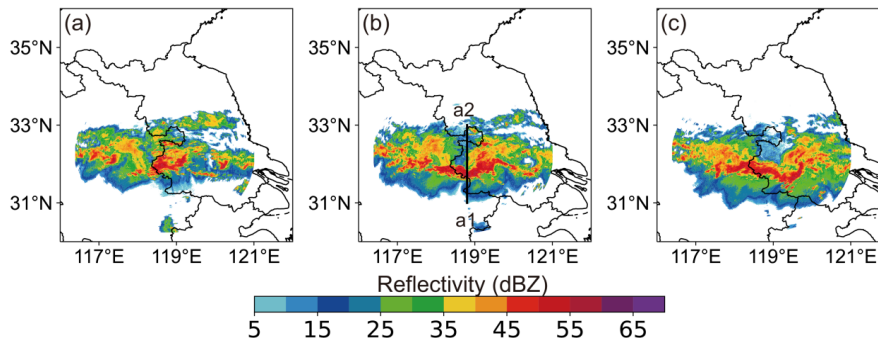
Fig. 2. The assimilation flow charts of Case 1 and Case 2.



210 4. Experimental results

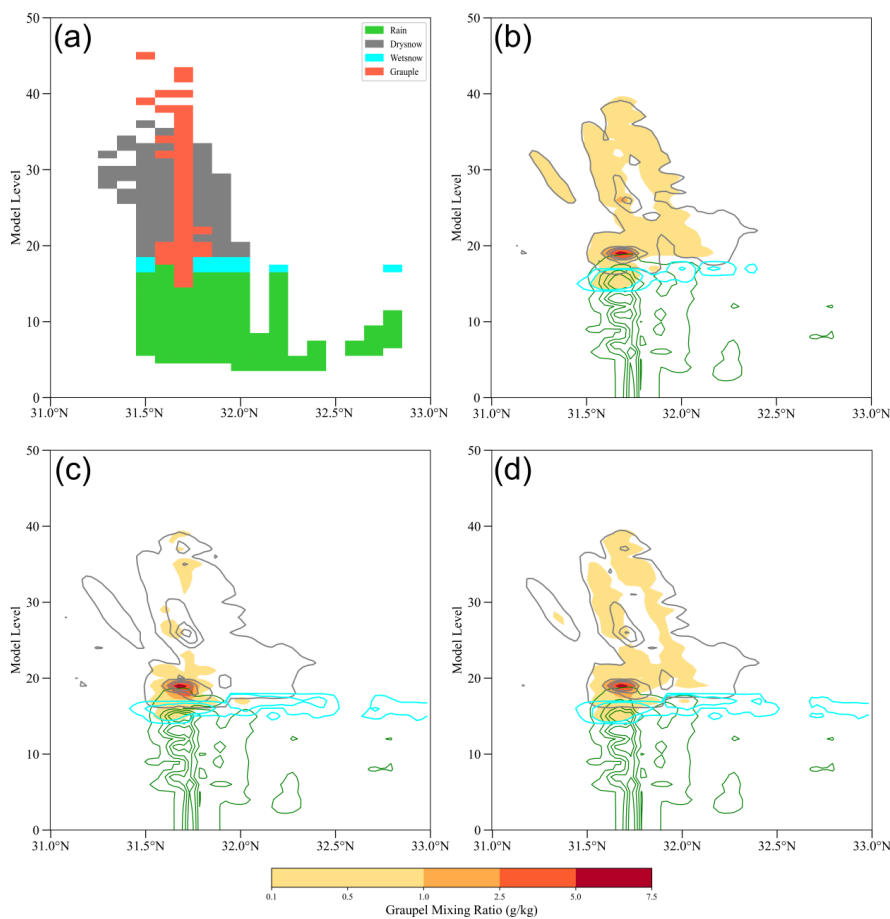
211 4.1 14 June 2020 case

212 Fig. 3 shows the observed reflectivity at 2300 UTC on 14 June, 0000 UTC, and 0100 UTC on 15
213 June 2020. At the beginning, there are strong echoes in the southwestern boundary of Jiangsu
214 Province. Subsequently, the strong convective band begins to expand in both eastward and westward
215 directions, stretching to the central Anhui Province and Jiangsu Province.



216
217 Fig. 3. The observed composite reflectivity fields (units: dBZ) at (a) 2300 UTC 14 June, (b) 0000 UTC, and (c)
218 0100 UTC 15 June 2020. The black line a1-a2 in the Fig. 3b is the vertical cross section location of Fig. 4.

219 Fig. 4 compares the Hydrometeor Classification Algorithm (HCA) based on dual-polarization
220 radar observations with the hydrometeor retrieval results from the three experiments at 1500 UTC
221 on June 14, 2020. The HCA diagram indicates that rainwater dominates the lower levels, while dry
222 snow and graupel prevail at higher levels, with wet snow present near the melting layer. In the
223 vertical cross sections of the three experiments (Figs. 4b, c, d), the overall distribution patterns of
224 the retrieved hydrometeors appear reasonable, especially for rain and snow. Notably, the wet snow
225 and graupel retrieved by EXP_temp-bg are more consistent with the HCA results compared to
226 EXP_temp and EXP_bg.



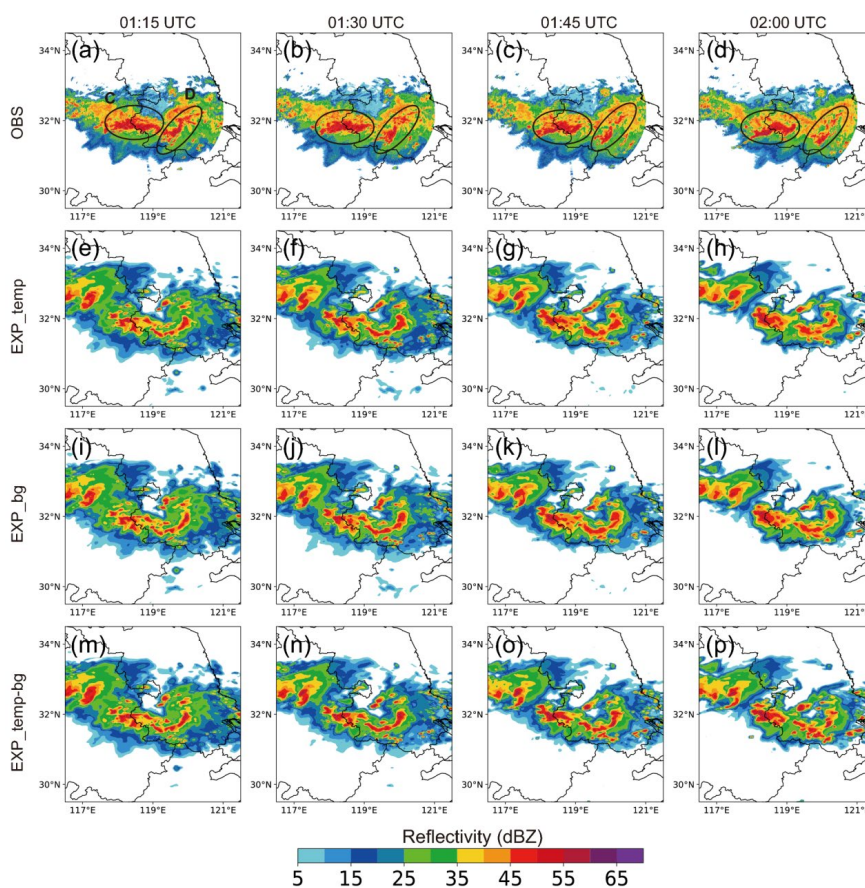
227

228 Fig. 4. The vertical sections of (a) hydrometeor classification algorithm based on the dual-polarization radar
229 observations and retrieved hydrometeors for (b) EXP_temp, (c) EXP_bg and (d) EXP_temp-bg along the black lines
230 a1-a2 at 1500 UTC. The retrieved hydrometeors refer to rainwater mixing ratio (green contours; units: dBZ), dry
231 snow mixing ratio (grey contours; units: dBZ), wet snow mixing ratio (cyan contours; units: dBZ), and graupel
232 mixing ratio (shading; units: dBZ), respectively.

233 To investigate the impact of the radar reflectivity DA based on the three hydrometeor retrieval
234 methods, Fig. 5 shows the predicted composite reflectivity initiated at 0100 UTC 15 June. It is
235 shown that the convective structure is divided into two parts (labeled C and D). From the
236 observations (Fig. 3a), the combination of C and D is initially located in the western Jiangsu and
237 eastern Anhui. Soon after, region D gradually separates from C and shifts eastward, displaying the
238 reduced intensity and poor organization. At 0115 UTC, all DA experiments are able to capture region



239 C and region D, albeit with slightly weaker intensity compared to the observations. At 0130 UTC,
240 the patterns of region C predicted by three experiments are depart from the observation, while the
241 echoes for EXP_temp-bg exhibit the best organization. At 0145 UTC, the regions C in EXP_temp
242 and EXP_bg show a poor agreement with the observations. In contrast, EXP_temp-bg provides
243 more accurate forecast in terms of shape and intensity. At 0200 UTC, three experiments can predict
244 region C and region D to some extent, but region D in EXP_temp-bg has most accurate echo pattern.
245 In general, the blending scheme is conducive to improving the radar reflectivity forecast skill.

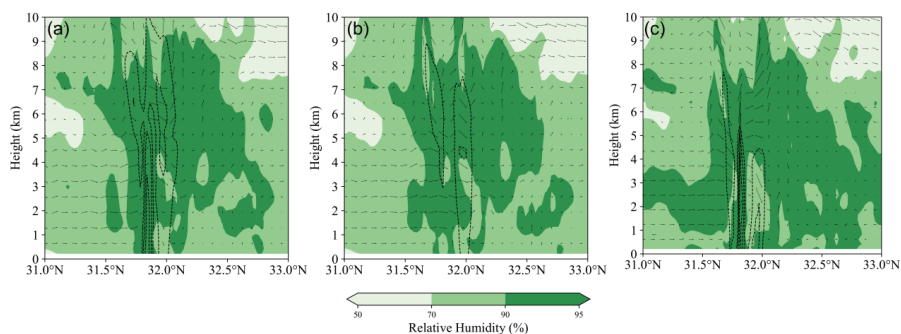


246
247 Fig. 5. The composite reflectivity (shaded; units: dBZ) predicted by (e)-(h) EXP_temp (i)-(l) EXP_bg and (m)-(p)
248 EXP_temp-bg for the 1-h forecast beginning at 0100 UTC 15 June 2020, as compared to (a)-(d) the observed
249 composite reflectivity. The labels C and D present the convection locations.

250 Fig. 6 displays the vertical cross sections of the relative humidity, radar reflectivity, and wind



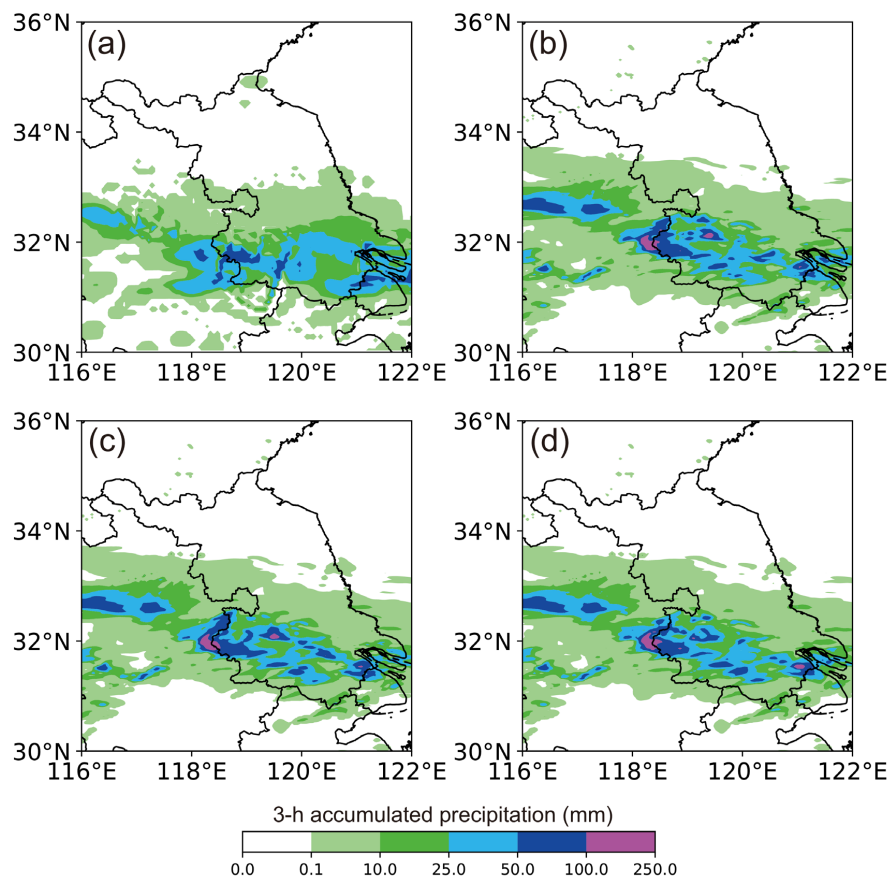
251 fields at 1501 UTC. After 1-hour forecast, the cross sections from all experiments indicate the
252 presence of saturated water vapor columns near the strong echoes (around 32°N). Notably,
253 EXP_temp-bg also reveals a robust updraft, facilitating the transport of water vapor from lower to
254 upper levels. In comparison, EXP_temp-bg produces the most consistent thermal and dynamical
255 conditions, resulting in most accurate forecast of the convection.



256
257 Fig. 6. The cross sections of relative humidity (shading; units: %), radar reflectivity (black contours starting at 40
258 dBZ; units: dBZ), and wind vectors for (a) EXP_temp, (b) EXP_bg and (c) EXP_temp-bg along the line a1-a2.

259 These are 1-hour forecasts initialized at 1501 UTC.

260 Fig. 7 shows the 3-h accumulated precipitation forecast from 1501 UTC to 1504 UTC on 15 June
261 2020. As depicted in Fig. 7a, the primary precipitation zone is concentrated along the western
262 boundary of Jiangsu Province, with accumulated precipitation exceeding 50mm. The precipitation
263 intensity is overestimated for three DA experiments. However, EXP_temp-bg effectively suppresses
264 two false precipitation areas, leading to the improved precipitation forecast.



265

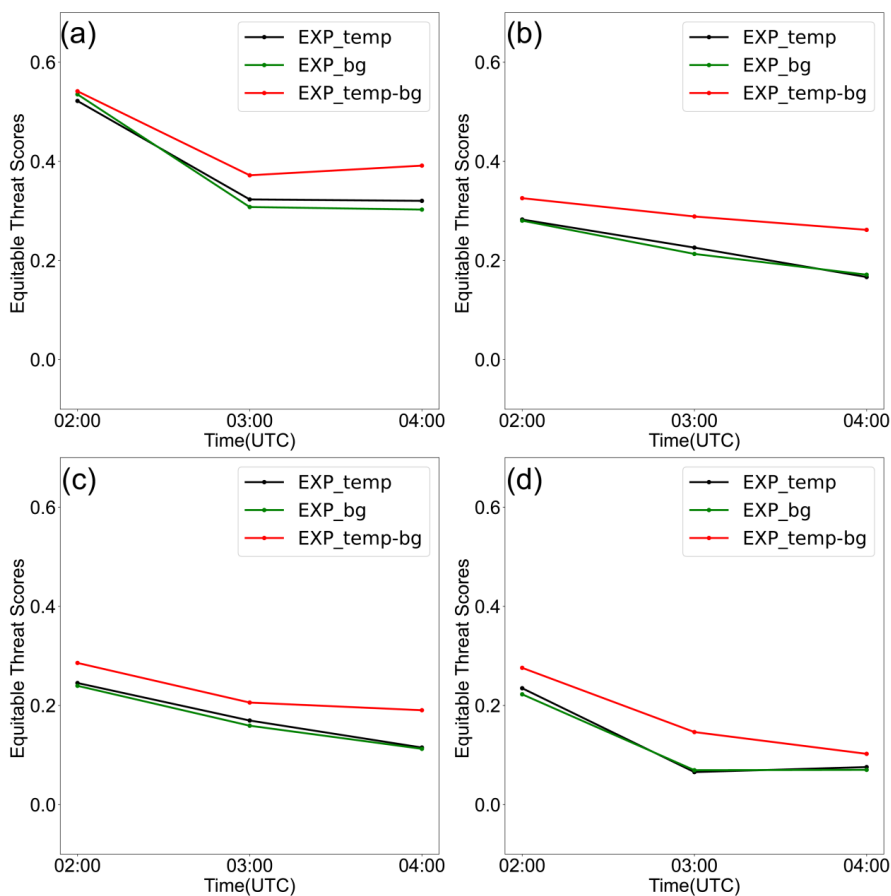
266 Fig. 7. 3-h accumulated precipitation valid at 0100 UTC 15 June 2020. (a) the observation, (b) EXP_temp, (c)

267

EXP_bg, and (d) EXP_temp-bg.

268

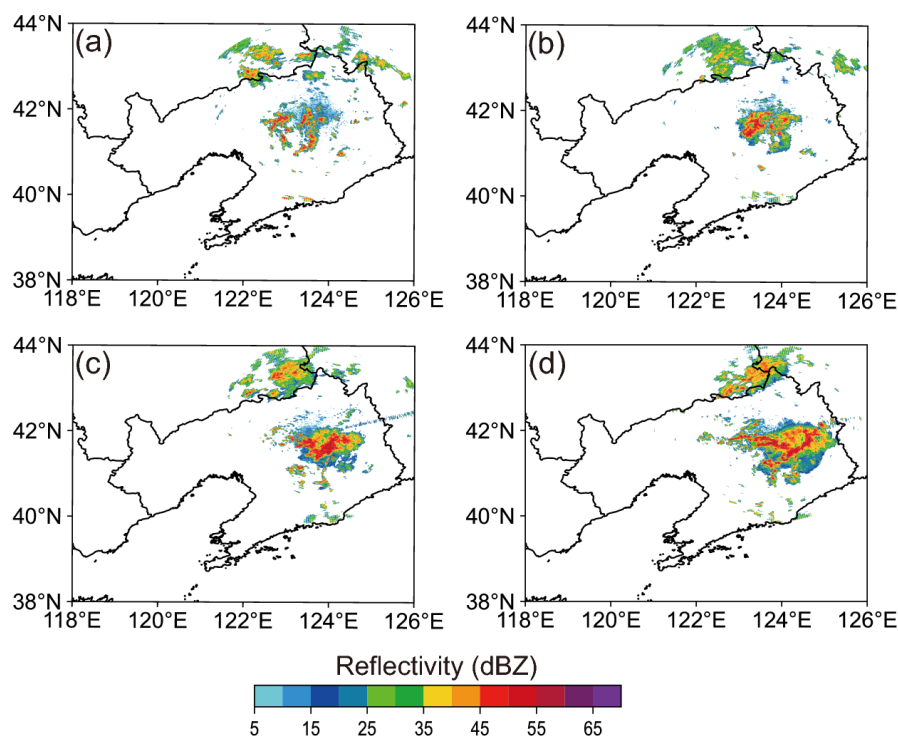
269 To quantitatively assess the performance of different hydrometeor retrieval schemes, the equitable
270 threat scores (ETS) are calculated for 0-3 h precipitation forecasts in EXP_temp, EXP_bg, and
271 EXP_temp-bg (Fig. 8). It is evident that as the precipitation threshold increases, the ETS values for
272 all three experiments decline progressively. Furthermore, EXP_temp and EXP_bg exhibit
273 comparable ETS values under various precipitation thresholds. In contrast, EXP_temp-bg
274 consistently outperforms both EXP_temp and EXP_bg for the entire 3-h forecast period, which
275 implies that the integrated hydrometeor retrieval scheme is conducive to the assimilation of radar
reflectivity observations.



276
277 Fig. 8. Equitable threat scores of hourly accumulated precipitation forecasts with five thresholds: (a) 0.1 mm, (b)
278 2.5 mm, (c) 5 mm and (d) 10 mm from 2300 UTC 14 June to 0100 UTC 15 June.

279 4.2 06 August 2018 case

280 Fig. 9 presents the observed composite reflectivity at 1800UTC, 1900UTC, 2000UTC, and
281 2100UTC on 06 August 2018. At 1800 UTC, there are a small number of strong radar echoes in the
282 central part of Liaoning Province. At 1900UTC, these discrete strong echoes gradually converge in
283 the center Liaoning, forming a well-organized structure. By 2000UTC, the convections continue to
284 develop and form into “V” pattern echo. At 2100UTC, a distinct “T” shaped echo emerges in the
285 observed area.



286

287 Fig. 9. The observed composite reflectivity fields (units: dBZ) at (a) 1800UTC, (b) 1900UTC, (c) 2000UTC and

288

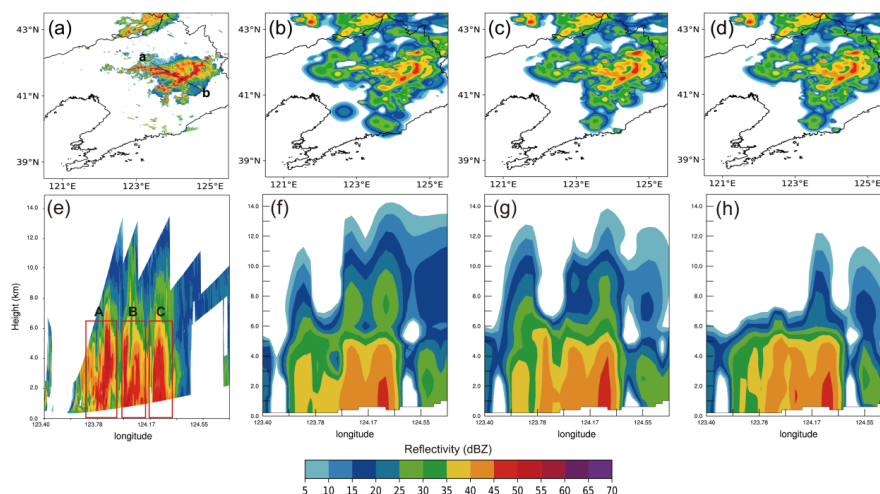
(d) 2100UTC 06 August 2018.

289

Fig. 10 shows the radar reflectivity analysis fields and the vertical cross sections along the line
290 ab from EXP_temp, EXP_bg, and EXP_temp-bg at 2100 UTC. As shown in Fig. 10a, a distinct “T”
291 shaped echo emerges in the observed area. Generally, the composite reflectivity analyses of the
292 experiments EXP_temp, EXP_bg, and EXP_temp-bg show a general agreement. From the observed
293 vertical cross section, it seems that there exist three strong echo bands between 123.78°E and
294 124.36°E. In order to display the differences between three DA experiments and the observation,
295 the convective system located near 123.75°E is marked as A, the strong convection at 123.97°E -
296 124.17°E is named as B, and the strong echo region at 124.17°E -124.36°E is labelled as C. Notably,
297 part A in the experiment EXP_temp departs from the observation, while EXP_bg and EXP_temp-
298 bg capture it more closely. Furthermore, the strong echo band analyzed by EXP_temp-bg indicates a
299 wider coverage than the one obtained from EXP_bg in part A. For part B, though all three DA
300 experiments exhibit a general agreement with the observation, their intensity is weaker than that in
301 the observation. It is found that EXP_temp-bg analyzes a strong center with reflectivity values



302 greater than 45dBZ for part B. All three experiments capture the overall structure of C. It seems
303 EXP_temp-bg combines the echo characteristics of both EXP_temp and EXP_bg in part C. On the
304 whole, EXP_temp-bg displays the advantages of fusion for most situations, matching best with the
305 observations.

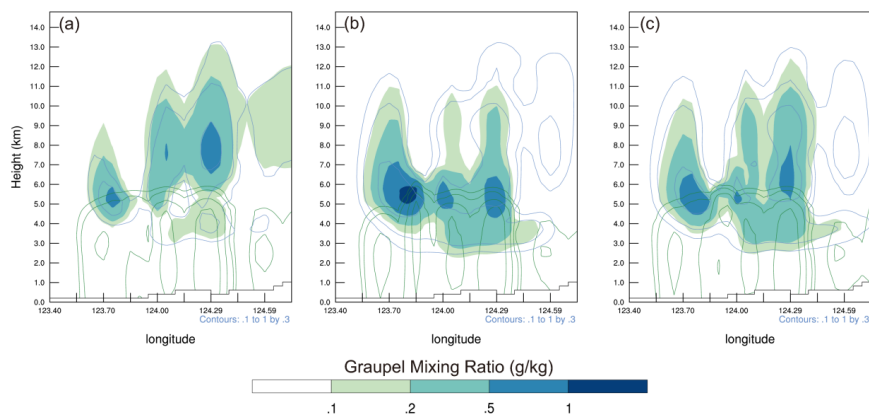


306
307 Fig. 10. The composite reflectivity at 2100 UTC for (a) observation, (b) EXP_temp, (c) EXP_bg, (d) EXP_temp-
308 bg, accompanied by the vertical cross sections for (e) observation, (f) EXP_temp, (g) EXP_bg, (h) EXP_temp-bg
309 along the line ab. The vertical cross section location at 2100UTC is shown by the line ab in the Fig. 10a. The labels
310 in the Fig. 10e present the convection locations.

311 To examine how different retrieval methods modify the hydrometeor distributions, the rainwater,
312 snow and graupel mixing ratio cross sections are presented in Fig. 11. Rainwater occurs below the
313 freezing level, while snow and graupel particles primarily exist above the freezing level. The
314 distribution of low-level rainwater in EXP_temp-bg is similar to that in EXP_bg. The proportion of
315 snow and graupel is a fixed coefficient in the EXP_temp, resulting in similar vertical distributions
316 as shown in Fig. 11a. However, it does not exist in the other two experiments with the “background
317 hydrometer-dependent” scheme. Additionally, both EXP_bg and EXP_temp-bg have significantly
318 higher snow and graupel content than EXP_temp. Fig. 11 shows three strong centers of graupel
319 particles corresponding to three strong reflectivity bands in the Fig. 10. By comparing the three
320 groups of the DA experiments, it is apparent that EXP_bg has the highest strong-center value, while
321 EXP_temp has the lowest. Moreover, the distribution of high-altitude hydrometeors in EXP_temp-



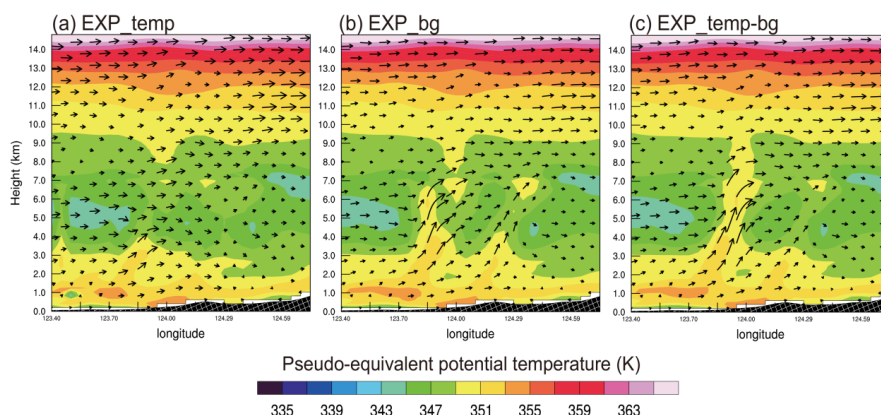
322 bg combines the features of EXP_temp and EXP_bg. To conclude, the hydrometeor vertical
323 distributions are closely related to the radar reflectivity structure as expected.



324
325 Fig. 11. The vertical cross sections of rainwater mixing ratio (green contours), snow mixing ratio (blue contours),
326 graupel mixing ratio (shading) at 2100 UTC for the experiments (a) EXP_temp, (b) EXP_bg, (c) EXP_temp-bg.

327 Fig. 12 displays the vertical cross sections of the pseudo-equivalent potential temperature (θ_{se}),
328 wind components, and reflectivity at 2100 UTC for EXP_temp, EXP_bg, and EXP_temp-bg. In the
329 three DA experiments, there exists a high θ_{se} zone in the lower layers (below 3 km), which shows
330 that a certain amount of energy has accumulated near the ground level. The area between 3 and 9
331 kilometers is characterized by a low θ_{se} zone, with the lowest value being below 343 K. Another
332 high θ_{se} zone exists above 10 kilometers. The results suggest that the vertical structure of the
333 atmosphere is unstable in this region, with dry conditions prevailing in the upper levels and moist
334 conditions in the lower levels. This type of vertical structure is favorable for the development of
335 severe convective weather events.

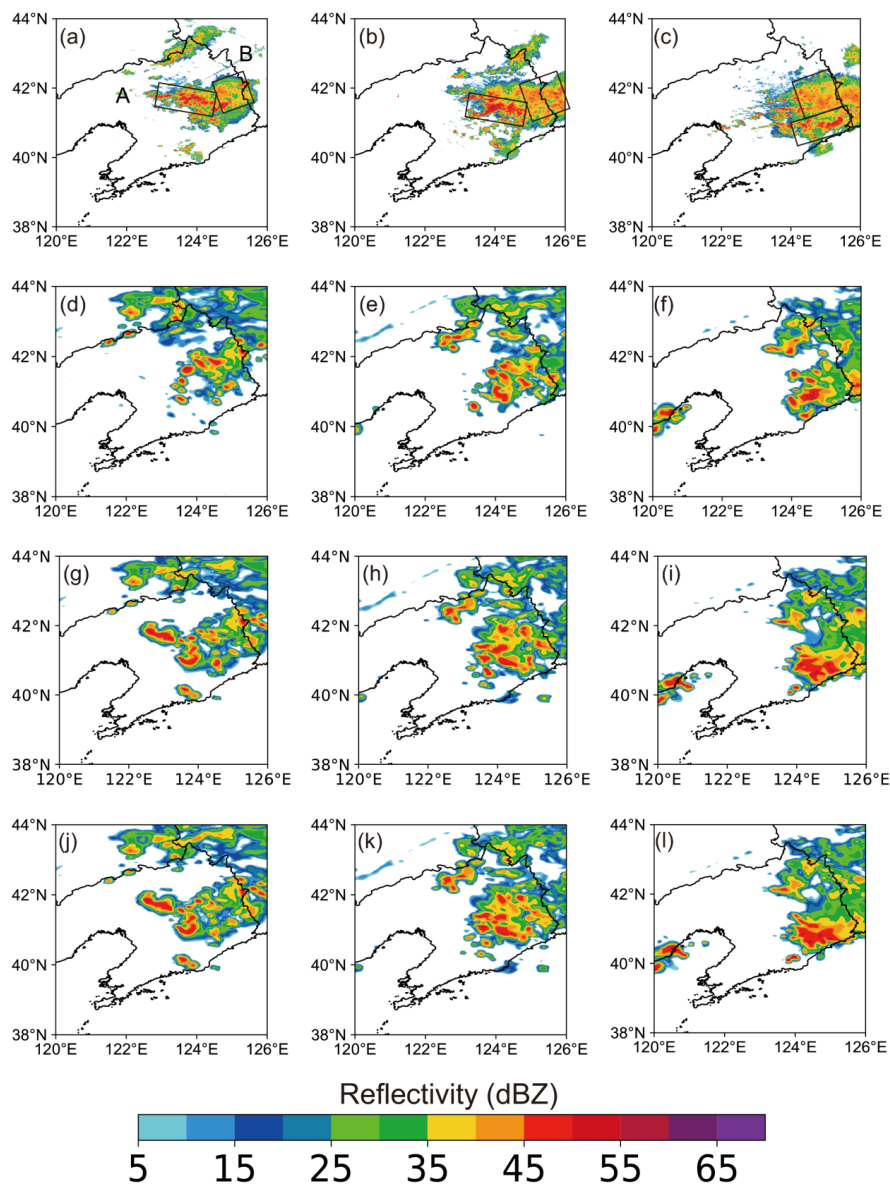
336 In the middle layer, there is a zone with relatively high θ_{se} value for EXP_bg and EXP_temp-bg.
337 Specifically, a warm-core structure is identified near 123.85°N, accompanied by strong upward
338 motion. This results in the release of unstable energy indicate that a severe convective system is
339 continuously developing. Additionally, compared with EXP_bg, EXP_temp-bg yields a more
340 extensive and deeper updraft column.



341

342 Fig. 12. The vertical sections of pseudo-equivalent potential temperature (shaded; units: K), velocity vectors (U,
343 W) at 2100 UTC for (a) EXP_temp, (b) EXP_bg and (c) EXP_temp-bg.

344 Fig. 13 shows 1-h, 3-h, and 5-h forecasts valid at 2100 UTC 06 August 2018 for EXP_temp,
345 EXP_bg, and EXP_temp-bg. As can be seen from the observation, the strong echo is located near
346 42°N at the beginning and has a tendency to slowly develop to the east. For the sake of clarity, the
347 strong echo zone is divided into two parts: part A and part B. At 2200 UTC 06 August, the forecasts
348 of three DA experiments for part B are inconsistent with the observation in terms of the intensity.
349 The part A predicted by EXP_bg and EXP_temp-bg shows a general agreement with the observation,
350 while the radar reflectivity forecast of EXP_temp departs from the observation. At 0000 UTC 07
351 August, EXP_bg and EXP_temp-bg yield an improved forecast for part A and B as compared with
352 EXP_temp, in terms of the intensity and organization. However, there is a southeast bias in part A
353 predicted by both EXP_bg and EXP_temp-bg. Compared to EXP_bg, EXP_temp-bg provides more
354 accurate predictions for part B. As shown by the observation at 0200 UTC 07 August, the predicted
355 A in EXP_temp-bg shows closer alignment with the observation than that in EXP_temp and
356 EXP_bg. For part B, three sets of experiments all depart from the observation. Overall, EXP_temp-
357 bg demonstrates superior prediction skills in terms of the radar reflectivity.

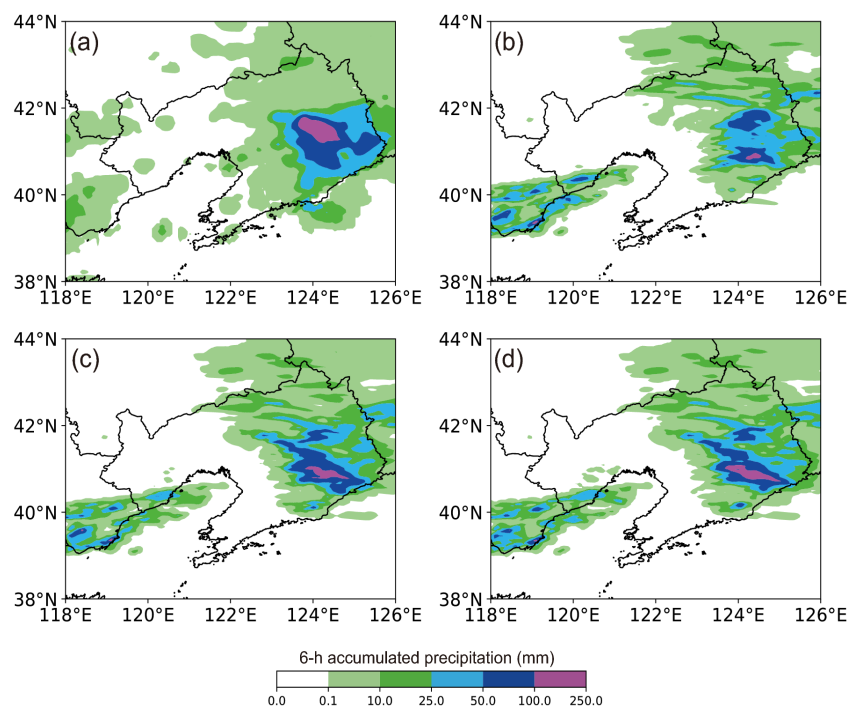


358
359 Fig. 13. The composite reflectivity (shaded; units: dBZ) predicted by (d)-(f) EXP_temp (g)-(i) EXP_bg and (j)-(l)
360 EXP_temp-bg, as compared to (a)-(c) the observed composite reflectivity. The corresponding times from left to
361 right are 2200 UTC 06 August (left), 0000 UTC 07 August (middle) and at 0200 UTC 07 August (right),
362 respectively. The labels A and B present the convection locations.

363 Fig. 14 shows 6-h accumulated precipitation of the three DA experiments from 2100 UTC 06



364 August to 0300 UTC 07 August 2018. According to the observation, heavy rainfall is mainly
365 concentrated in the northeastern part of Liaoning, with precipitation amount exceeding 100 mm. All
366 three experiments underestimate the extent of the precipitation in this event, especially in the range
367 of 25 mm to 50 mm. Moreover, there is a certain deviation between the predicted and observed
368 locations. As shown in Fig. 9c and d, the patterns of heavy precipitation areas are similar in EXP_bg
369 and EXP_temp-bg. EXP_bg and EXP_temp-bg are notably better than EXP_temp in predicting the
370 rainfall for the threshold 50mm. EXP_temp-bg displays the best forecasting skill in terms of the
371 heavy rainfall area.



372
373 Fig. 14. 6-h accumulated precipitation valid at 2100 UTC 06 August 2018. (a) the observation, (b) EXP_temp, (c)
374 EXP_bg, and (d) EXP_temp-bg.

375 5. The conclusion

376 The study proposes an adaptive hydrometeor retrieval scheme within the WRF-3DVar system,
377 which combines “temperature-based” and “background hydrometer-dependent” methods to
378 enhance the analyses and forecasts for the strong convections. In the indirect assimilation of radar



379 reflectivity, it is vital to correctly divide hydrometeor information in radar reflectivity. On the basis
380 of two retrieval methods proposed by Gao and Stensrud (2012) and Chen et al. (2020, 2021), the
381 blending scheme is developed to minimize the limitations brought by both methods so as to improve
382 the assimilation and prediction skills.

383 The above three hydrometeor retrieval schemes are evaluated for two strong convective processes
384 occurred during June 2020 and August 2018. Three DA experiments (EXP_temp, EXP_bg, and
385 EXP_temp-bg) are conducted by using the “temperature-based”, “background hydrometer-
386 dependent”, and blending methods, respectively. The analysis results reveal that the blending
387 method is effective to improve the radar reflectivity structures for severe convections. Based on the
388 other two DA experiments, EXP_temp-bg further improves hydrometeor structures and properly
389 allocates the proportion of each hydrometeor, which is responsible for more reasonable hydrometeor
390 distributions. Also, EXP_temp-bg provides more reasonable dynamic and thermal structures
391 compared with EXP_temp and EXP_bg. EXP_temp-bg shows advantages in the precipitation
392 prediction skills due to the reasonable spatial distribution and proportion of each hydrometeor.

393 Compared to conventional Doppler weather radars, dual-polarization radar observations provide
394 more accurate identification of the three-dimensional microphysical structures within precipitation
395 systems. Consequently, dual-polarization radar data will be considered for hydrometeor retrievals
396 in our future studies, aiming to further enhance the forecast skills for severe weathers.

397

398 **Data availability**

399 The GFS reanalysis data is available at <https://rda.ucar.edu/datasets/ds084.1/>, and the source code
400 of WRF and WRFDA can be downloaded from <https://github.com/wrf-model>. The radar
401 observations after quality control are provided by Jiangsu and Liaoning Provincial Meteorological
402 Bureau, and the precipitation observations can be found at
403 [http://data.cma.cn/dataService/cdcindex/datacode/NAFP_CLDAS2.0_NRT/show_value/normal.ht](http://data.cma.cn/dataService/cdcindex/datacode/NAFP_CLDAS2.0_NRT/show_value/normal.html)
404 [ml](http://data.cma.cn/dataService/cdcindex/datacode/NAFP_CLDAS2.0_NRT/show_value/normal.html).

405

406 **Author contribution**

407 LS: visualization, writing (original draft). FS: conceptualization, writing (review and editing). ZH:



408 conceptualization, methodology. DX: writing (review and editing). AS: visualization. JC: software.

409

410 **Competing interests**

411 The contact author has declared that none of the authors has any competing interests.

412

413 **Acknowledgments**

414 This research was primarily supported by the Chinese National Natural Science Foundation of China
415 (G42192553), the China Meteorological Administration Tornado Key Laboratory (TKL202306), Natural
416 Science Fund of Anhui Province of China under grant (2308085MD127), the Open Grants of China
417 Meteorological Administration Radar Meteorology Key Laboratory (2023LRM-B03), the Open Project
418 Fund of China Meteorological Administration Basin Heavy Rainfall Key Laboratory (2023BHR-Y20),
419 the Shanghai Typhoon Research Foundation (TFJJ202107), the Chinese National Natural Science
420 Foundation of China (G41805070). We acknowledge the High Performance Computing Center of
421 Nanjing University of Information Science & Technology for their support of this work.

422 **References**

- 423 Bick, T., Simmer, C., Trömel, S., et al. 2016: Assimilation of 3D radar reflectivities with an ensemble
424 Kalman filter on the convective scale. *Quart. J. Roy. Meteor. Soc.*, 142(696), 1490-1504.
- 425 Borderies, M., Caumont, O., Delanoë, J., et al. 2019: Impact of airborne cloud radar reflectivity data
426 assimilation on kilometre-scale numerical weather prediction analyses and forecasts of heavy
427 precipitation events. *Natural Hazards and Earth System Sciences*, 19(4), 907-926.
- 428 Chen, F., Dudhia, J. 2001: Coupling an advanced land surface-hydrology model with the Penn State-
429 NCAR MM5 modeling system. Part I: Model implementation and sensitivity. *Monthly Weather*
430 *Review*, 129, 569-585.
- 431 Chen, H., Chen, Y., Gao, J., et al. 2020: A radar reflectivity data assimilation method based on
432 background-dependent hydrometeor retrieval: An observing system simulation experiment.
433 *Atmospheric research*, 243, 105022.
- 434 Chen, H., Gao, J., Wang, Y., et al. 2021: Radar reflectivity data assimilation method based on
435 background-dependent hydrometeor retrieval: Comparison with direct assimilation for real
436 cases. *Quart. J. Roy. Meteor. Soc.*, 147(737), 2409-2428.



- 437 Chen, J., Xu, D., Shu, A., et al. 2023: The Impact of Radar Radial Velocity Data Assimilation Using
438 WRF-3DVAR System with Different Background Error Length Scales on the Forecast of Super
439 Typhoon Lekima (2019). *Remote Sensing*, 15(10), p.2592.
- 440 Courtier, P., Thépaut, J. N., Hollingsworth, A. 1994: A strategy for operational implementation of
441 4D-Var, using an incremental approach. *Quart. J. Roy. Meteor. Soc.*, 120(519), 1367-1387.
- 442 Dowell, D. C., Wicker, L. J., Snyder, C. 2011: Ensemble Kalman filter assimilation of radar
443 observations of the 8 May 2003 Oklahoma City supercell: Influences of reflectivity
444 observations on storm-scale analyses. *Monthly Weather Review*, 139(1), 272-294.
- 445 Dudhia, J. 1989: Numerical study of convection observed during the winter monsoon experiment
446 using a mesoscale, two-dimensional model. *Journal of the Atmospheric Sciences*, 46, 3077-
447 3107.
- 448 Evensen, G. 1994: Sequential data assimilation with a nonlinear quasi-geostrophic model using
449 Monte Carlo methods to forecast error statistics. *Journal of Geophysical Research: Oceans*,
450 99(C5), 10143-10162.
- 451 Gao, J., Xue, M., Brewster, K., et al. 2004. A three-dimensional variational data analysis method
452 with recursive filter for Doppler radars. *Journal of Atmospheric and oceanic technology*, 21(3),
453 457-469.
- 454 Gao, J., Stensrud, D. J. 2012: Assimilation of reflectivity data in a convective-scale, cycled 3DVAR
455 framework with hydrometeor classification. *Journal of the Atmospheric Sciences*, 69(3), 1054-
456 1065.
- 457 Gustafsson, N., Janjić, T., Schraff, C., et al. 2018: Survey of data assimilation methods for
458 convective-scale numerical weather prediction at operational centres. *Quart. J. Roy. Meteor.*
459 *Soc.*, 144(713), 1218-1256.
- 460 Hong, S. Y., Noh, Y., Dudhia, J. 2006: A new vertical diffusion package with an explicit treatment
461 of entrainment processes. *Monthly Weather Review*, 134, 2318-2341.
- 462 Hu, M., Xue, M., Brewster, K. 2006: 3DVAR and cloud analysis with WSR-88D level-II data for
463 the prediction of the Fort Worth, Texas, tornadic thunderstorms. Part I: Cloud analysis and its
464 impact. *Monthly Weather Review*, 134, 675-698.
- 465 Huang, L., Xu, D., Li, H., et al. 2023: Assimilating FY-3D MWHS2 Radiance Data to Predict



- 466 Typhoon Muifa Based on Different Initial Background Conditions and Fast Radiative Transfer
467 Models. *Remote Sensing*, 15(13), p.3220.
- 468 Kain, J. S., Xue, M., Coniglio, M. C., et al. 2010: Assessing advances in the assimilation of radar
469 data and other mesoscale observations within a collaborative forecasting-research environment.
470 *Weather and forecasting*, 25(5), 1510-1521.
- 471 Kong, R., Xue, M., Liu, C. 2018: Development of a hybrid En3DVar data assimilation system and
472 comparisons with 3DVar and EnKF for radar data assimilation with observing system
473 simulation experiments. *Monthly Weather Review*, 146(1), 175-198.
- 474 Kong, R., Xue, M., Liu, C., et al. 2020: Comparisons of hybrid En3DVar with 3DVar and EnKF for
475 radar data assimilation: Tests with the 10 May 2010 Oklahoma tornado outbreak. *Monthly*
476 *Weather Review*, 149(1), 21-40.
- 477 Li, X., Ming, J., Wang, Y., et al. 2013: Assimilation of T-TREC-retrieved wind data with WRF
478 3DVAR for the short-term forecasting of typhoon Meranti (2010) near landfall. *Journal of*
479 *Geophysical Research: Atmospheres*, 118(18), 10-361.
- 480 Li, X., Zeng, M., Wang, Y., et al. 2016: Evaluation of two momentum control variable schemes and
481 their impact on the variational assimilation of radar wind data: Case study of a squall line.
482 *Advances in Atmospheric Sciences*, 33, 1143-1157.
- 483 Lindskog, M., Salonen, K., Järvinen, H., et al. 2004: Doppler radar wind data assimilation with
484 HIRLAM 3DVAR. *Monthly weather review*, 132(5), 1081-1092.
- 485 Lilly, D. K. 1990: Numerical prediction of thunderstorms-Has its time come? *Quart. J. Roy. Meteor.*
486 *Soc.*, 116, 779-798.
- 487 Liu, C., Xue, M., Kong, R. 2019: Direct assimilation of radar reflectivity data using 3DVAR:
488 Treatment of hydrometeor background errors and OSSE tests. *Monthly Weather Review*,
489 147(1), 17-29.
- 490 Lopez, P. 2011: Direct 4D-Var assimilation of NCEP stage IV radar and gauge precipitation data at
491 ECMWF. *Monthly Weather Review*, 139(7), 2098-2116.
- 492 Mlawer, E., Taubman, S., Brown, P., et al. 1997: Radiative transfer for inhomogeneous atmospheres:
493 RRTM, a validated correlated-k model for the longwave. *Journal of Geophysical Research*,
494 102, 16663-16682.



- 495 Navon, I. M. 2009: Data assimilation for numerical weather prediction: a review. *Data assimilation*
496 for atmospheric, oceanic and hydrologic applications, 21-65.
- 497 Parrish, D. F., Derber, J. C. 1992: The National Meteorological Center's spectral statistical-
498 interpolation analysis system. *Monthly Weather Review*, 120(8), 1747-1763.
- 499 Schenkman, A. D., Xue, M., Shapiro, A., et al. 2011: The analysis and prediction of the 8-9 May
500 2007 Oklahoma tornadic mesoscale convective system by assimilating WSR-88D and CASA
501 radar data using 3DVAR. *Monthly Weather Review*, 139(1), 224-246.
- 502 Shen, F., Min, J., Xu, D. 2016: Assimilation of radar radial velocity data with the WRF Hybrid
503 ETKF--3DVAR system for the prediction of Hurricane Ike (2008). *Atmospheric Research*, 169,
504 127-138.
- 505 Shen, F., Xu, D., Min, J. 2019: Effect of momentum control variables on assimilating radar
506 observations for the analysis and forecast for Typhoon Chanthu (2010). *Atmospheric Research*
507 234, 104771.
- 508 Shen F., Xu, D., Li, H., et al. 2020a: Impact of radar data assimilation on a squall line over the
509 Yangtze–Huaihe River Basin with a radar reflectivity operator accounting for ice-phase
510 hydrometeors. *Meteorol Appl.* 28, e1967.
- 511 Shen, F., Xu, D., Min, J., et al. 2020b: Assimilation of radar radial velocity data with the WRF
512 hybrid 4DVar system for the prediction of hurricane Ike (2008). *Atmospheric research*, 234,
513 104771.
- 514 Shen, F., Min, J., Li, H., et al. 2021: Applications of radar data assimilation with hydrometeor control
515 variables within the wrfda on the prediction of landfalling hurricane ike (2008). *Atmosphere*,
516 12(7), 853.
- 517 Shen, F., Song, L., Li, H., et al. 2022: Effects of different momentum control variables in radar data
518 assimilation on the analysis and forecast of strong convective systems under the background
519 of northeast cold vortex. *Atmospheric Research*, 280, 106415.
- 520 Simonin, D., Ballard, S. P., Li, Z. 2014: Doppler radar radial wind assimilation using an hourly
521 cycling 3D-Var with a 1.5 km resolution version of the Met Office Unified Model for
522 nowcasting. *Quart. J. Roy. Meteor. Soc.*, 140(684), 2298-2314.
- 523 Sun, J., Crook, N.A. 1997: Dynamical and microphysical retrieval from Doppler radar observations



524 using a cloud model and its adjoint. Part I: Model development and simulated data experiments.
525 *Journal of the Atmospheric Sciences*, 54(12), 1642-1661.

526 Sun, J., Xue, M., Wilson, J. W., et al. 2014: Use of NWP for nowcasting convective precipitation:
527 Recent progress and challenges. *Bulletin of the American Meteorological Society*, 95(3), 409-
528 426.

529 Tong, M., Xue, M. 2005: Ensemble Kalman filter assimilation of Doppler radar data with a
530 compressible nonhydrostatic model: OSS experiments. *Monthly Weather Review*, 133, 1789-
531 1807.

532 Tong, C. C., Jung, Y., Xue, M., et al. 2020: Direct assimilation of radar data with ensemble Kalman
533 filter and hybrid ensemble-variational method in the National Weather Service operational data
534 assimilation system GSI for the stand-alone regional FV3 model at a convection-allowing
535 resolution. *Geophysical Research Letters*, 47(19), e2020GL090179.

536 Wan, S., Shen, F., Chen, J., et al. 2024: Evaluation of Two Momentum Control Variable Schemes in
537 Radar Data Assimilation and Their Impact on the Analysis and Forecast of a Snowfall Case in
538 Central and Eastern China. *Atmosphere*, 15(3), 342.

539 Wang, H., Sun, J., Fan, S., et al. 2013a: Indirect assimilation of radar reflectivity with WRF 3D-Var
540 and its impact on prediction of four summertime convective events. *Journal of Applied
541 Meteorology and Climatology*, 52, 889-902.

542 Wang, H., Sun, J., Zhang, X., et al. 2013b: Radar data assimilation with WRF 4D-Var. Part I: System
543 development and preliminary testing. *Monthly Weather Review*, 141(7), 2224-2244.

544 Xiao, Q., Kuo, Y. H., Sun, J., et al. 2005: Assimilation of Doppler radar observations with a regional
545 3DVAR system: Impact of Doppler velocities on forecasts of a heavy rainfall case. *Journal of
546 Applied Meteorology*, 44(6), 768-788.

547 Xiao, Q., Kuo, Y. H., Sun, J., et al. 2007: An approach of radar reflectivity data assimilation and its
548 assessment with the inland QPF of Typhoon Rusa (2002) at landfall. *Journal of Applied
549 Meteorology and Climatology*, 46(1), 14-22.

550 Xu, D., Shen, F., & Min, J. 2019: Effect of adding hydrometeor mixing ratios control variables on
551 assimilating radar observations for the analysis and forecast of a typhoon. *Atmosphere*, 10(7),
552 415.



- 553 Xu, D., Shu, A., Li, H., et al. 2021: Effects of Assimilating Clear-Sky FY-3D MWHS2 Radiance on
554 the Numerical Simulation of Tropical Storm Ampil. *Remote Sensing*, 13(15), 2873.
- 555 Xu, D., Yang, G., Wu, Z., et al. 2022: Evaluate radar data assimilation in two momentum control
556 variables and the effect on the forecast of southwest China vortex precipitation. *Remote*
557 *Sensing*, 14(14), 3460.
- 558 Zhao, K., Li, X., Xue, M., et al. 2012: Short-term forecasting through intermittent assimilation of
559 data from Taiwan and mainland China coastal radars for Typhoon Meranti (2010) at landfall.
560 *Journal of Geophysical Research: Atmospheres*, 117(D6).